The Astrophysical Journal, 703:1–7, 2009 September 20 doi:10.1088/0004-637X/703/1/1

A CORONAL MASS EJECTION AND HARD X-RAY EMISSIONS ASSOCIATED WITH THE KINK INSTABILITY

Kyung-Suk Cho[1], Jeongwoo Lee[2], Su-Chan Bong[1], Yeon-Han Kim[1], Bhuwan Joshi[3], and Young-Deuk Park[1]
[1] Korea Astronomy and Space Science Institute, Daejeon, 305-348, Korea; kscho@kasi.re.kr
[2] Center for Solar-Terrestrial Research, New Jersey Institute of Technology, Newark, NJ 07102, USA
[3] Udaipur Solar Observatory, Physical Research Laboratory, Udaipur 313001, India
Received 2009 March 9; accepted 2009 July 7; published 2009 August 25

ABSTRACT

We present a morphological study of the 2004 August 18 solar eruption that occurred in the active region NOAA 10656 near the west limb using extreme-ultraviolet (EUV) data from the *Transition Region and Coronal Explorer* (*TRACE*), Hα filtergram of Big Bear Solar Observatory, white light images of Mauna Loa Solar Observatory (MLSO), hard X-ray (HXR) data of the *Reuven Ramaty High Energy Solar Spectroscopic Imager* (*RHESSI*), and microwave data of the Owens Valley Solar Array. In this event, we have an excellent set of observations for tracing the early evolution of the coronal mass ejection (CME) from a flux rope emergence to its propagation into space as a well-connected series of events thanks to the coronameter's field of view (FOV) down to 1.1 solar radius in an overlap with that of the *TRACE*. This data set reveals continuously evolving EUV, Hα, and WL features that suggest the rise of a small, low-lying loop, its writhing motion, break of the kinked loop at its crossing point, and transformation of the ejecta to the CME. The HXR and microwave sources are found in varying locations with a complicated temporal dependence, which, we interpret, is due to two successive flares in the event. The first flare appears to be associated with the rise of the small loop, which then triggers the second flare. During the second flare a HXR coronal source is detected at the crossing point of the kinked loop, and more intriguingly, the kinked loop apparently breaks at the crossing point of the two legs, which indicates a magnetic reconnection at the X-point configuration. After the break of the kinked UV loop, a CME structure shows up in the MLSO FOV, and propagates away from the Sun. It is concluded that this CME occurred due to the kink instability.

Key words: Sun: coronal mass ejections (CMEs) – Sun: flares – Sun: X-rays, gamma rays

Online-only material: animation

1. INTRODUCTION

Eruption mechanisms for the coronal mass ejections (CMEs) are currently a hot topic in solar physics and solar–terrestrial relation studies. For several decades, association of CMEs with solar flares as a driver has been a focus of the debates (Kahler 1992; Gosling 1993; Harrison 1995; Hundhausen 1997, 1999). More recent studies have converged to a common view that both CME and flare react to each other in a constructive way via magnetic reconnections, and thus the cause–effect relation seems to be no longer important (e.g., Zhang & Dere 2006). However, exactly what role is played by magnetic reconnection in solar eruptions still varies depending on theoretical models. For instance, the role of magnetic reconnection in a so-called tether cutting model is to remove tethers so that a flux rope can be released (Moore et al. 2001). In the magnetic break-out model, first reconnection should occur in a higher corona to remove overlying flux so that a low-lying flux tube can rise (Antiochos et al. 1999). In these cases, the reconnection is thus necessary as a trigger for the eruption, in which sense it should precede the eruption. Magnetic reconnection can also play a role in increasing the poloidal field of a flux rope by transferring neighboring flux into itself, thus allowing the flux rope to form and grow (van Ballegooijen & Martens 1990). On the other hand, another class of eruption models, called catastrophe models, assumes that a system slowly evolves, as an ideal MHD process, to a stage where no more equilibrium exists and a rapid eruption follows. In this case, the primary cause for the eruption is the loss of MHD equilibrium, and magnetic reconnection may occur as a secondary effect during the rapid structural change of the system (see the review by Lin et al. 2003). Confronting these two groups of theoretical ideas with observations may be hard because of limited time cadence and spatial coverage, but certainly needs to be made.

In this paper, we present an observational study of one event in which the morphology is indicative of magnetic kink evolution. Because of the kink-like features, we will interpret the observation against the magnetic kink instability models (Fan 2005; Török & Kliem 2003, 2005), paying our main attention to the exact relationship of the reconnection with the kinking process. Observationally, the kinked magnetic structure has been studied in many papers. The first detailed study of the evolving kink structure is probably that of the so-called "failed" CME event (Ji et al. 2003). Several studies have followed to discuss the kink formation (Williams et al. 2005), relative timing of kinked loop eruption and flares (Liu et al. 2007c), and the location of hard X-ray (HXR) sources in kinking filaments (Alexander et al. 2006; Liu & Alexander 2009). We revisit these issues with the present data set. One advantage of our data set is that the field of view (FOV) of the Mauna Loa Solar Observatory (MLSO) MK4 coronameter (from 1.1 to 2.8 $R_{\odot}$; Elmore et al. 2003) covers the low corona enough to overlap with the *TRACE* limb observation. Such spatial coverage would be vitally important in detecting the transformation of an erupting filament into a CME. We thus expect to investigate more clearly the association between flares and the CME with this data set.

2. DATA

The 2004 August 18 eruption occurred in the west limb (S14 W90) active region, NOAA 10656. For morphological

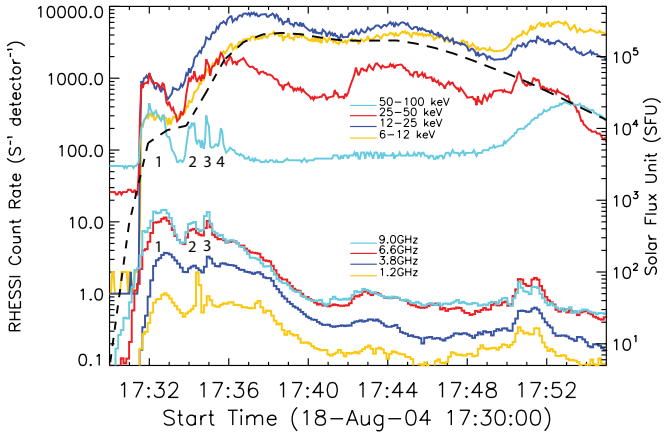

Figure 1. Time profiles of the flare in *GOES* 10 X-ray flux (0.5–4.0 Å), *RHESSI* hard X-ray (6–12, 12–25, 25–50, and 50–100 keV), and OVSA microwave (1.2, 3.8, 6.6, and 9.0 GHz). Marked numbers represent the flare time. The sharp transition at about 17:31:32 UT is the instrumental effect due to the end of eclipse for *RHESSI* at 17:31:20 UT, as evidenced by the radio light curves. Note that an attenuator state change from A3 to A1 at 17:31:44 UT affects the count rates at lower energies.

investigation of the prominence emergence and eruption, we use *TRACE* (Handy et al. 1999) 195 Å and 1600 Å together with Hα filtergram obtained from Big Bear Solar Observatory (BBSO). The *TRACE* data have pixel resolution of 0.″5 and time cadence of ∼1 minute for 1600 Å or better for a 195 Å filter. BBSO full disk Hα data used in this study are acquired with the telescope equipped with a 2032×2032 pixel Apogee KX4 detector with spatial resolution of about 1″ pixel^{-1} and time resolution of 1 minute. The associated CME was detected by the MLSO MK4 coronameter. The MK4 coronameter observe white-light (WL) brightness at every 3 minutes in the wavelength range from 700 to 950 nm (Elmore et al. 2003). The pixel resolution of the MK4 coronameter is about 5.″93.

The flare gained the *GOES* class X1.8. Figure 1 shows the *RHESSI* HXR light curves (at 6–12, 12–25, 25–50, and 50–100 keV) and the OVSA microwave time profiles (at 1.2, 3.8, 6.6, and 9.0 GHz). All light curves show multiple peaks between 17:32 (UT) and 17:40 (UT) which we distinguish by numbers. The first flare occurred near 17:32 and has relatively longer duration, while the other three HXR peaks have very short durations. It is interesting that the last peak ("4") of the HXR has no corresponding radio peak. At low energies (⩽50 keV) HXR emission seems to continue even after 17:34 UT, which is presumably due to thermal bremsstrahlung radiation.

3. THE OBSERVED ERUPTION PROCESS

We describe the morphological changes using Hα and EUV images around peaks 1–4 in Figure 1 taken as times of intense energy release via magnetic reconnection. We then present the measurement of the CME as detected in the MLSO coronameter to complete the description of the eruption process.

3.1. Emergence of a Flux Rope

We use the BBSO full disk Hα data to examine the changes in the early phase of the eruption (17:20–17:34 UT). In this period, there is a *TRACE* data gap from 17:22:11 UT to 17:34:04 UT. Hα images are shown in Figure 2. In the first frame (a), we can see an Hα loop at 17:32 UT. In the next two frames (b,c) this loop simply grows out in height. In the next frame (d), the morphology no longer implies a simple loop, and it looks rather

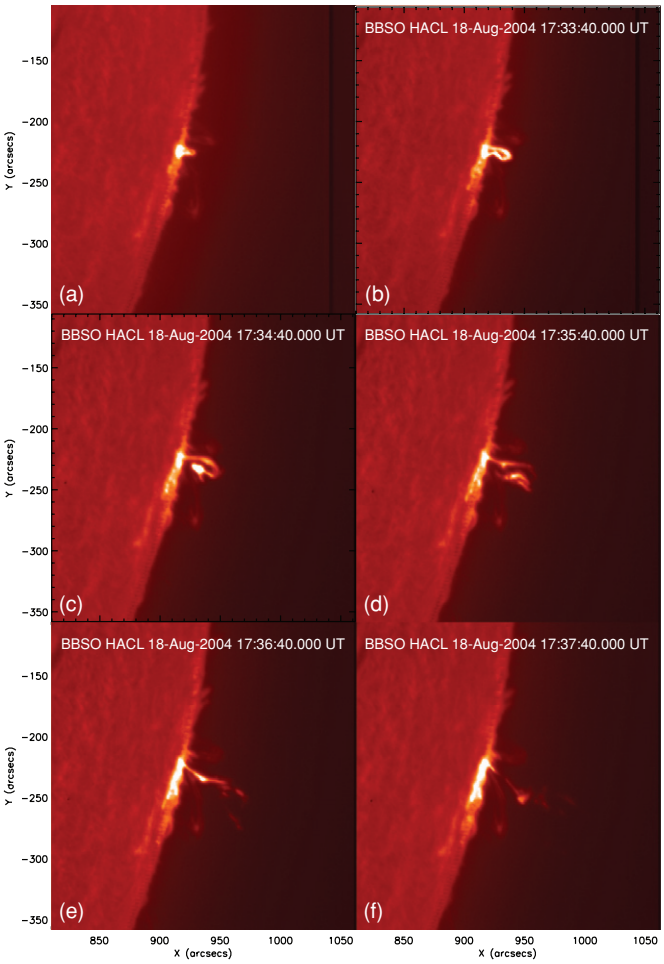

Figure 2. BBSO Hα images showing the early phase of the prominence eruption. Emerging loop evolving into a kinked loop is observed during the entire period of flares from 17:31 to 17:36 UT.

like a twisted loop (17:35:40 UT). In the last two frames (e,f) a thin vertical structure appears, which seems to connect the rising bright source to its footpoints.

These Hα images clearly show that some magnetic structure started to emerge after the first flare (peak 1 in Figure 1). It is, however, not very clear to us what the evolving features represent. It is our impression from the Hα movie that this great eruption started with a small, low-lying loop rather than a large pre-existing prominence. However, it is also possible that the loop appears to be small, as it has partly been occulted by the limb. The possibility of the limb occultation will further be discussed with the *RHESSI* maps later in this section. Another puzzle is whether the rising bright feature in the early phase (Figure 2(a)) is a prominence or a post-flare loop. While such a bright feature can be a post-flare loop, it could also be a bright prominence (Liu et al. 2007c) perhaps due to heating (Filippov & Koutchmy 2002). In any case, it is likely that its brightness and rising motion should be associated with the first flare emission at 17:31:30 UT (peak 1 in Figure 1).

3.2. Kink Development and Eruption

Figure 3 shows the morphological evolution in the *TRACE* EUV at 195 Å that are available after 17:34 UT. The overall impression is the same as in Hα images (Figure 2) except that EUV features appear in a fine filamentary structure and correspond to higher temperature ∼MK. Especially in the

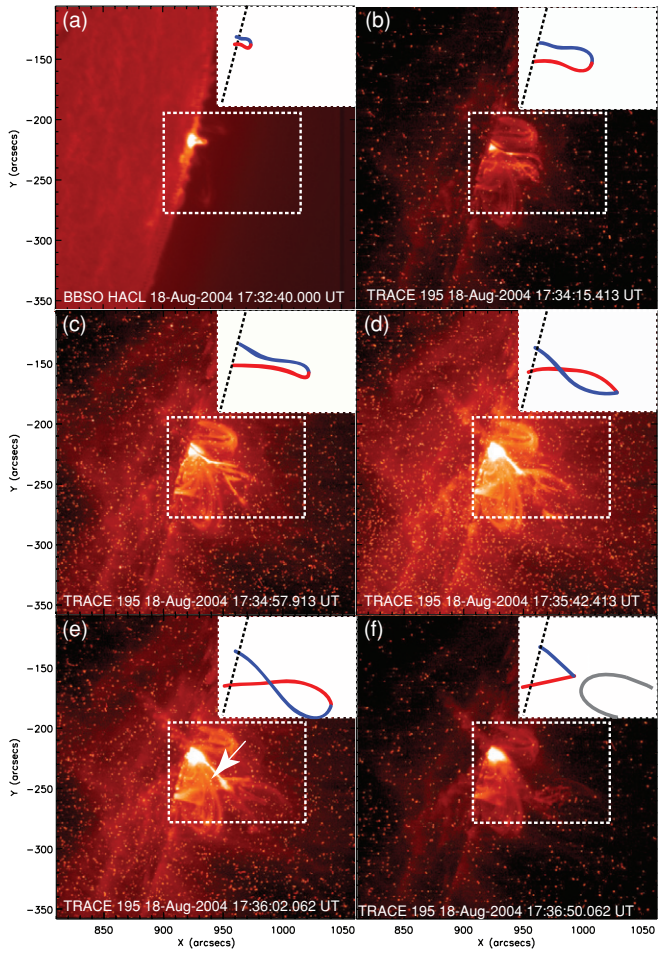

Figure 3. Morphological changes of the prominence observed with *TRACE* 195 Å filter. A brief inset sketch is deduced from the prominence in the dotted box. The blue line represents the visible part of the prominence and the red line denotes the unseen part of the prominence.

second frame (Figure 3(b)), a bright core is located near the surface and a thin structure stands above it, similar to what we have seen in Hα (Figure 2). In the next frames (c–d), the loop not only grows in height but also develops a writhe (i.e., a kinked loop in α shape), as illustrated by the insets in the upper right corner of each panel. With these EUV images alone, we may not ascertain whether the EUV feature is really of a continuous twisted loop or just a projection of several loops that happen to aligned in that shape. We however believe that the former is likely because we have seen that this twisted feature has evolved from a closed Hα loop. This complicated morphology probably results as a mixture of a kink-unstable flux tube and another group of the arcade field lines wrapping the flux rope became bright. In this interpretation, the observed morphological changes in Figure 3 would represent the development of the kink, and it indeed resembles the snapshots of the kink instability model by Török & Kliem (2005, their Figure 4).

Another noticeable feature is the bright thin feature standing above the bright core (indicated by an arrow in Figure 3(e)). This was present in Hα and is more clearly seen in EUV. The fact that it is also seen in EUV 195 Å means that this is associated with heating during the flare. If we compare this to the standard magnetic reconnection model (Priest & Forbes 2002), the thin vertical feature may be in the position corresponding to a current sheet where the magnetic reconnection occurs and the thin and bright features are the current sheet itself. An alternative interpretation would be that the bright thin structure is aligned along one leg of the kinked loop. This is then the same phenomenon as the brightening sheaths along the kinked filament legs, as reported by Ji et al. (2003).

3.3. Transformation of Prominence to CME

The associated CME was detected by the MLSO MK4 coronameter (see, for more detailed description of the CME, Cho et al. 2007). In Figure 4, we show the *TRACE* UV images for the details of the flares in upper panels. The bottom panel is a composite image of the CME and flare, where a frame of *TRACE* UV (image in red) is shown together with a vignetted MK4 CME images (blue-colored image) taken between 17:41 and 17:44 UT. The actual FOV of the MK4 starts at about 1.1 $R_{\odot}$ and has an overlap with the chromospheric observations by *TRACE* UV. The images belong to two different times. The UV image is the last visible ejecta, while the WL images the first available frame that shows the CME structure. When the CME structure appears, the CME already has well defined three part structures: core, void, and front. The rest of the MLSO/MK4 images show that the bright CME core propagates away from the Sun. While the core propagates, the flare region on the solar surface is diminishing out. A movie showing the transformation of the prominence to the CME can be found in the electronic version of this paper.

To calculate the kinematics, we need to set a reference point in both prominence (Hα–EUV images) and CME (WL images). Where to set the reference point is illustrated in Figure 4. Before the CME appears, we measure the bottom of the feature that we consider as the flux rope. These points are marked by the arrows in the *TRACE* UV images (Figure 4, upper panels). After the CME appears, we set the reference point at the bottom of the core as denoted by an arrow in Figure 4, the lower panel, since we believe this point should correspond to that of the flux rope seen in the *TRACE* UV images.

3.4. CME Dynamics

The heights of the above measured points in Figure 4 are plotted as a function of time in Figure 5. The symbols show the motion of the erupting prominence (plus and triangle symbols) and that of the CME core (diamond and square symbols). The corresponding velocity is shown in the lower panel in comparison with X-ray light curves. The solid black curve is *GOES* soft X-ray flux, and the colored curve is the *RHESSI* light curves at a 50–100 keV (sky) channel, respectively. The error bars in the symbols are estimated by assuming two pixel measurement error of the *TRACE* 1600 Å and MLSO/MK4 data, respectively. The kinematic evolution of the prominence is characterized by the slow emergence of a flux rope ($\leqslant$50 km s^{-1}) up to the distance of 10 Mm (time 1, 2, and 3). After rapid acceleration $\sim$1.5 km s^{-2} up to 100 Mm, it propagates with constant velocity (400 km s^{-1}) beyond 400 Mm. The pattern of slow rising, rapid acceleration, and constant speed is as typical as predicted by most eruption models (e.g., Priest & Forbes 2002, their Figure 20(a)).

Of interest in the height–time diagram is derivation of the CME acceleration for comparison with flare emission. We are quite convinced about the height measurement, as the heights were carefully checked both by the eyes and by an automatic routine. The resulting height–time curve of the UV feature smoothly continues to that of the CME, which gives

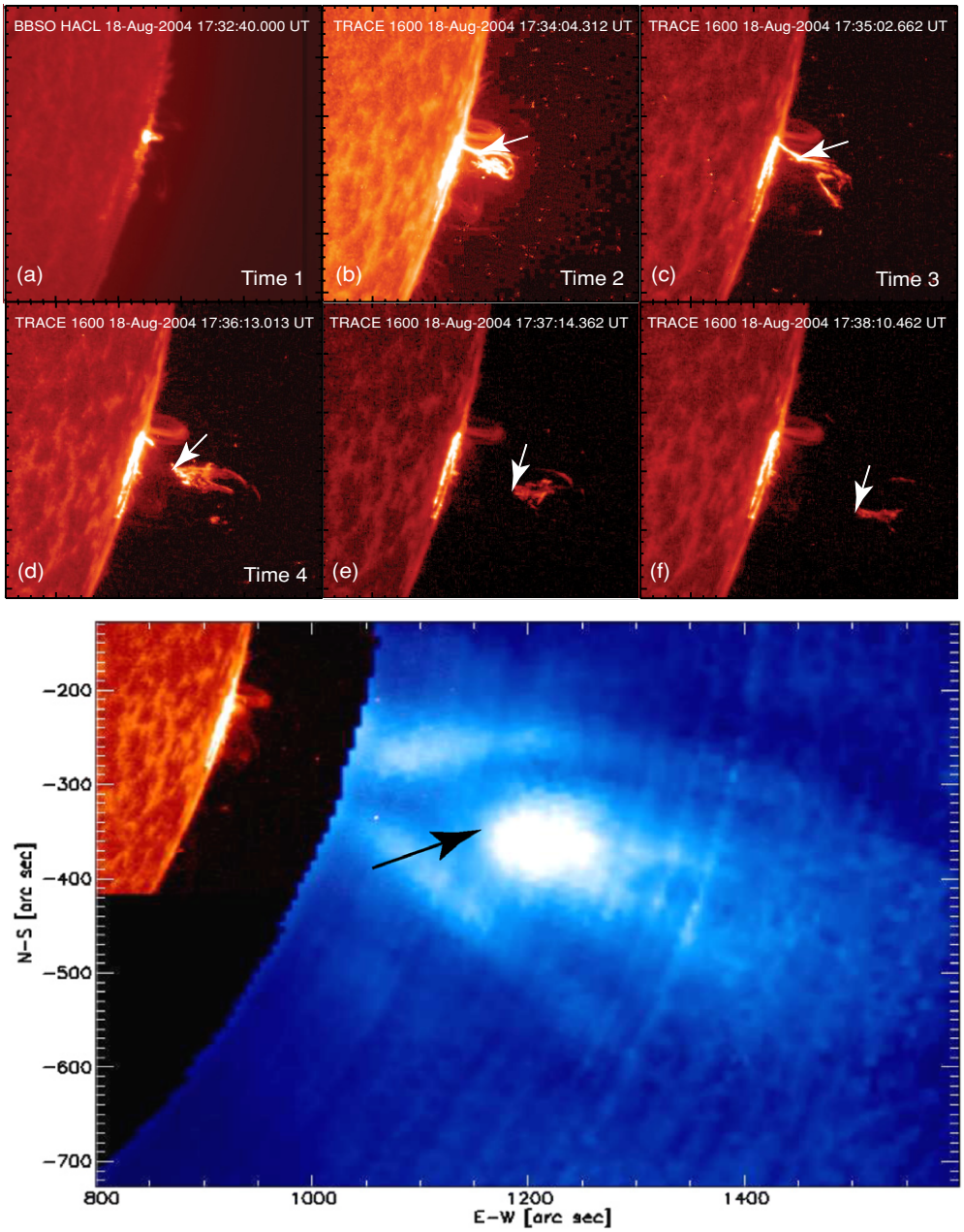

Figure 4. Continuous evolution of the prominence to the CME. Upper panels: *TRACE* UV images of the prominence evolution. Bottom: a composite image of flare and CME with *TRACE* 1600 Å at 17:41:34 UT (red-colored image) and MLSO MK4 white light CME image at 17:44:32 UT (blue-colored image). When this CME with the three part structure first appeared in the MLSO coronameter, the flare on the solar surface had already faded out.

(An animation of this figure is available in the online journal.)

another support for the result. Nevertheless, it is still tricky to determine the acceleration of CME as it requires the second-order difference, and large errors can be introduced. We instead check the most obvious feature in the velocity curve only. As we can see in the figure, velocities are crudely determined due to the limited number of data points. The time when velocity begins to rise (i.e., start of acceleration) is hardly determined. But the time when the velocity becomes nearly constant (i.e., cease of acceleration) can be roughly estimated to be at 17:39–17:40 UT. This is close to the maximum of the *GOES* soft X-ray light curve (17:38 UT), which agrees to what Zhang et al. (2001, 2004) have found. Implied is that the maximum acceleration would be close to the the HXR peak related to the soft X-ray peak, as confirmed in a few occasions (Temmer et al. 2008).

3.5. HXR Emission

The HXR maps are reconstructed by using the CLEAN algorithm from the *RHESSI* data in 12–25 keV (blue contours), 25–50 keV (red), and 50–100 keV (sky blue) channels, respectively. The integration time is 1 minute. Shorter integration time is doable but does not lead to a very different images. They are shown against *TRACE* UV (1600 Å) in Figure 6. In the early time around the emerging prominence (Figure 6(a)), we see two HXR sources denoted by A and B. Although source A is seemingly slightly above the limb, with this image alone, it is hard to tell whether A–B is a combination of looptop and footpoint sources or both are footpoints. However, a couple of properties suggest that A is likely of a coronal source. First, A appears

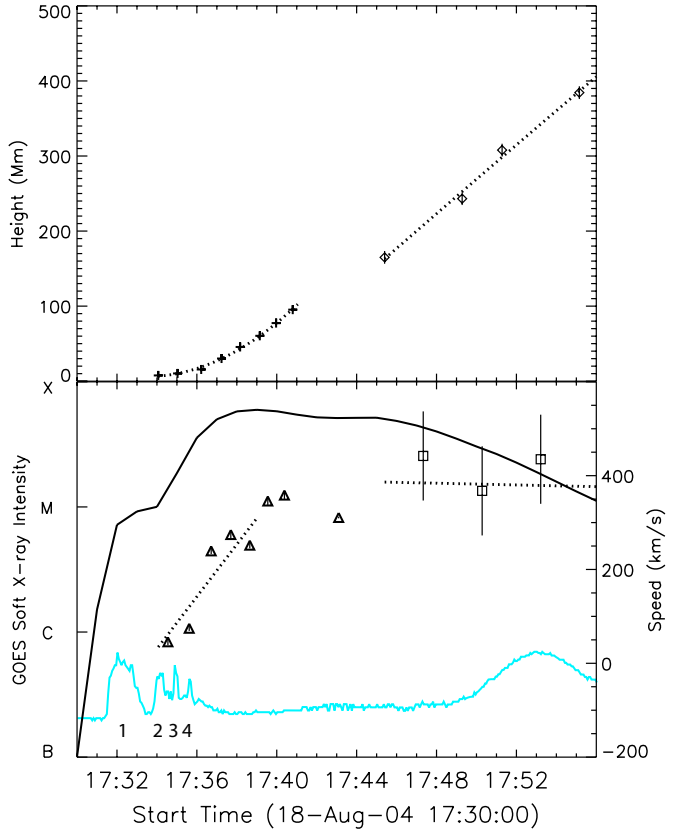

Figure 5. Height–time data of the bottom of the prominence as denoted by the arrows in Figure 4. The height and the velocity are estimated from *TRACE* (plus and triangle symbols) and MLSO MK4 (diamond and square symbols) data. A solid black curve in the lower panel is the *GOES* 10 X-ray flux (0.5–4.0 Å) curve and colored line is *RHESSI* hard X-ray (HXR) in 50–100 keV (sky) channel. The four peaks in the light curve are marked for a comparison between the flare time and the prominence kinematics.

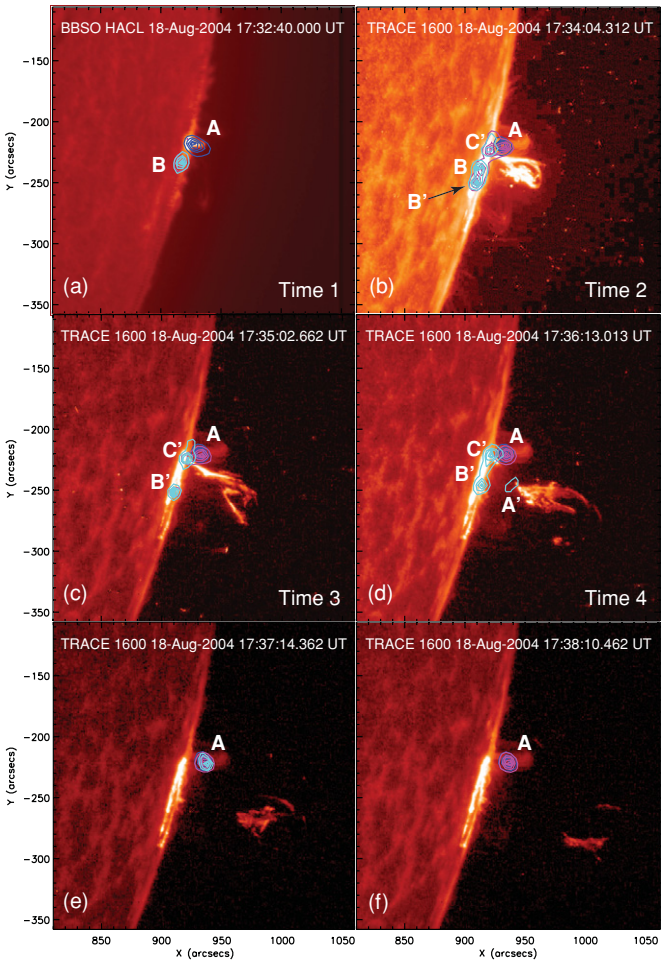

Figure 6. Positions of the *RHESSI* HXR sources labeled are overlayed on BBSO Hα image (a) and *TRACE* UV 1600 Å images (b–f). The HXR sources are labeled by the uppercase. The contour levels are 50%, 70%, 80%, 90%, and 95% of the peak intensity for three energy bands: 12–25 keV (blue), 25–50 keV (red), and 50–100 keV (sky). Flare times assigned in Figure 1 are denoted in panels (a) to (d).

at lower photon energies (12–25 keV) than B (50–100 keV). Second, A appears in a consistent position and keeps moving upward slowly during the rest of the event, which is a frequently observed feature of HXR coronal sources (Sui & Holman 2003). B is concurrent with A and only appears in the nonthermal energy range (50–100 keV), and it is likely that B is a footpoint source. The other footpoint conjugate to B probably lies over the limb not to be detected.

Later morphology around the source B becomes complicated. Either the source B evolves from a single to double sources that extends and shrinks from time to time or other footpoint sources newly appear around source B while B itself vanishes. We argue in favor of the latter scenario because the light curves shown in Figure 1 are suggestive of two flares in this event. First of all, the *GOES* soft X-ray light curve as well as the 6–12 keV *RHESSI* light curve shows a double peak features: one at 17:30 UT and the other at 17:40 UT. This implies the presence of two flares. In addition, the HXR emission corresponding to peak 1 shows similar time profiles for different energy bands, while those during peaks 2–4 are impulsive only at higher energies and gradual at lower energies. It is thus likely that there are two separate flares corresponding to the double soft X-ray peaks. In this interpretation, it is more reasonable to postulate that the second flare involves another loop A′–B′–C′ rather than assuming that A′–B′–C′ is a later development of the same loop A–B (Figures 6(b)–(d)). Since A′ is certainly a coronal source, B′ and C′ are likely of conjugate footpoints to each other in view of their relative positions (Figure 6(d)).

Identifying the HXR sources in this way, several important features are found. (1) The coronal source, A′, is located at the crossing point of the kinked loop (Figure 6(d)), reminiscent of a similar flare morphology reported by Alexander et al. (2006) and Liu & Alexander (2009). The conjugate footpoint sources, B′ and C′, during peaks 2–4 are located at the endpoints of the kinked loop. (2) Unlike other failed eruptions (e.g., Ji et al. 2003), the kinked loop apparently *breaks* at the crossing point of the two legs (Figure 6(e)), indicating magnetic reconnection at an X-point configuration. This strongly suggests that the same field line reconnects on itself, and that the corresponding coronal source is expected to be very impulsive and nonthermal. Indeed source A′ is found at much higher photon energies compared with other looptop sources previously reported (cf. 20–50 keV of the coronal source reported by Masuda et al. 1994; Sui & Holman 2003). It may be that the coronal source, A′, could be detected at the high photon energy band because some of the footpoint emissions were partly occulted by the limb.

3.6. Microwave Emission

Figure 7 shows a radio map that was reconstructed with the CLEAN algorithm and the 30 s accumulated data between

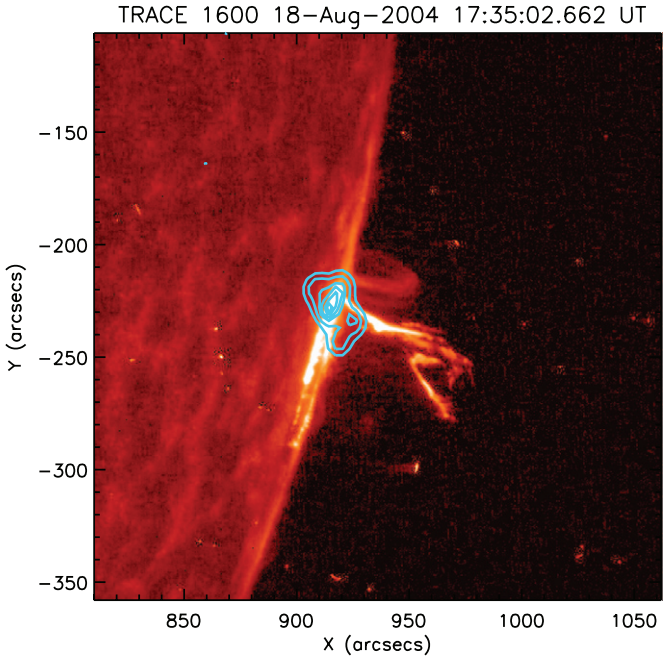

Figure 7. OVSA radio image in 8.6–9.4 GHz frequency band taken during 17:34:30–17:35:00 UT. Positions of the radio source at different time ranges (time 1, and 2) are similar to each other. No radio source in the band is seen during the eruption (time 4).

17:34:30 (UT) and 17:35:00 (UT) and using frequency synthesis over 8.6–9.4 GHz with center frequency at 9.0 GHz, and is shown as contours overlaid on the *TRACE* UV image at the third flare peak (time 3). We made radio maps at other frequencies too, but the sources show up in the common place without a considerable change in morphology. This radio source location is similar to the position of the HXR foot-point sources. Radio sources do not show well resolved footpoint sources and other features like transformation of the footpoint-like emission to ribbon-like emissions for the footpoint sources B′–C′. But it is also sensitive to the magnetic field, and thus the radio sources are considered to represent the footpoint sources where energetic electrons and strong magnetic field are.

3.7. Magnetic Structure

Finally, we check the above reconnection scenario against the actual magnetic configuration of this active region as shown in Figure 8. The active region, NOAA 10656, was quite prolific in producing flares. On 2004 August 13, it produced an X-class flare, and from that day onward, about 20 M-class flares, and then the X-class flare on August 18. The magnetogram taken three days before the event shows the polarity inversion line (PIL) in a complicated shape, close to the so-called S-shape in sigmoid. It is rather common in this type of configuration that the first flare starts from the inner sheared core via tether cutting and then the disturbance propagates out to produce successive flares (Liu & Zhang 2001; Moore et al. 2001).

Based on the above idea, we propose the following scenario for this event. The inner core near the PIL was so complicated and produced the first flare via a reconnection between the low-lying, core field lines, and this explains why the loop A–B is such a small loop. The reconnection in this case is typically of tether cutting, which can trigger successive flares. As a result, the next three HXR peaks occurred in another loop in view of the *RHESSI* maps. Similarly, Alexander et al. (2006) and Liu & Alexander (2009) also reported HXR sources (12–25 keV) located around kinked loops and interpreted them as due to either magnetic reconnections between the legs or with the field lines wrapping around the prominence. The coronal HXR source in this event may differ from them in that it appears in the X-point which formed as the same field line reconnected on itself.

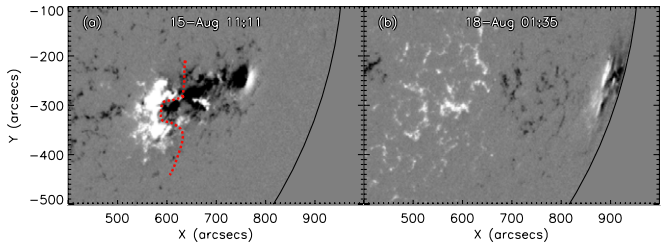

Figure 8. Line-of-sight MDI magnetogram of the AR NOAA 10656. Left: the magnetogram taken three days earlier than the event shows a complicated magnetic polarity distribution on the surface. The red line is an estimated polarity inversion line. Right: the magnetogram of the active region on the day of the eruption studied in this paper.

Observational support for this scenario comes from the HXR, microwave and EUV maps. First, we observed that the footpoints of the legs of this kinked loop appeared as the HXR footpoint sources and a radio source (B′ and C′), and the corresponding coronal source (source A′) appeared at the location expected to be the breaking point. Another feature frequently found in this type of the complex active region is the sigmoid-to-arcade transformation (Liu et al. 2007a, 2007b), which results in the change of HXR sources from a more confined, footpoint sources to ribbon-like HXR sources. The complicated evolution of the footpoints B–B′–C′ may represent a sigmoid-to-arcade transformation observed near the limb.

4. SUMMARY

We have presented a multiwavelength study of the 2004 August 18 eruption to find a few distinct behaviors in the morphological evolution of Hα and EUV features and HXR-microwaves sources during this event. First, the EUV kinked loop has continuously evolved from a small, low-lying Hα loop, which suggests the rise of a flux rope, its writhing motion, and break of the kinked loop at its crossing point. These morphological changes suggest kink evolution, as much as other observations did (Ji et al. 2003; Romano et al. 2003), except that it started with a small Hα structure rather than a noticeably large, pre-existing prominence structure. A theoretical model that comes close to the present observation is that of Török & Kliem (2005) not only for the apparent similarity of the observed morphologies of the EUV and Hα with the magnetic kink model, but for the overall evolution pattern consisting of slow rise, a helical structure development, and eruption. We therefore conclude that this eruption was caused by the kink instability. Second, the HXR sources appear in varying locations with a complicated time dependence, which, we interpret, is due to the presence of two successive flares in this event. The first flare is apparently associated with an emerging small flux rope, and may have triggered the second flare. During the second flare, conjugate footpoints are located at the endpoints of the kinked loop, and the corresponding coronal source is found at the crossing point of the kinked loop, reminiscent of a similar flare morphology reported by Alexander et al. (2006) and Liu & Alexander (2009). The associated coronal source is very impulsive and energetic, as expected for a magnetic

reconnection at the X-point beneath the erupting flux rope. Of the multiple HXR peaks, the last peak should be associated with the X-type magnetic reconnection, while the other preceding peaks are probably due to reconnections among legs of kinking flux ropes. To our knowledge, this is the first report of the break of the kinked loop and HXR sources around it, which evidences the magnetic kink instability as a mechanism for solar eruptions.

We thank the anonymous referee for many critically important comments, especially, on the interpretation of the HXR and Hα data. We also thank Rui Liu for helpful comments. This work has been supported by the "Development of Korean Space Weather Center" of KASI and the KASI basic research funds. OVSA was supported by the NSF grant AST-0607544 and NASA grant NNG06GJ40G to NJIT. The Mauna Loa Solar Observatory (MLSO) is operated by the High Altitude Observatory (HAO), a division of the National Center for Atmospheric Research (NCAR), which is sponsored by the National Science Foundation (NSF).

REFERENCES

Alexander, D., Liu, R., & Gilbert, H. R. 2006, ApJ, 653, 719
Antiochos, S. K., DeVore, C. R., & Klimchuk, J. A. 1999, ApJ, 510, 485
Cho, K.-S., Lee, J., Moon, Y.-J., Dryer, M., Bong, S.-C., Kim, Y.-H., & Park, Y. D. 2007, A&A, 461, 1121
Elmore, D. F., Burkepile, J. T., Darnell, J. A., Lecinski, A. R., & Stanger, A. L. 2003, Proc. SPIE, 4843, 66
Fan, Y. 2005, ApJ, 630, 543
Filippov, B., & Koutchmy, S. 2002, Sol. Phys., 208, 283
Gosling, J. T. 1993, J. Geophys. Res., 98, 18937
Handy, B. N., et al. 1999, Sol. Phys., 187, 229
Harrison, R. A. 1995, A&A, 304, 585
Hundhausen, A. J. 1997, in Cosmic Winds and the Heliosphere, ed. J. R. Jokipii, C. P. Sonett, & M. S. Giampapa (Tuscon, AZ: Univ. Arizona Press), 259
Hundhausen, A. J. 1999, in The Many Faces of the Sun: A Summary of the Results from NASA's Solar Maximum Mission, ed. K. T. Strong et al. (New York: Springer), 143
Ji, H., Wang, H., Schmahl, E. J., Moon, Y.-J., & Jiang, Y. 2003, ApJ, 595, L135
Kahler, S. W. 1992, ARA&A, 30, 113
Lin, J., Soon, W., & Baliunas, S. L. 2003, New Astron. Rev., 47, 53
Liu, C., Lee, J., Gary, D., & Wang, H. 2007a, ApJ, 658, L127
Liu, C., Lee, J., Yurchyshyn, V., Deng, N., Cho, K.-S., Karlicky, M., & Wang, H. 2007b, ApJ, 669, 1372
Liu, R., & Alexander, D. 2009, ApJ, submitted
Liu, R., Alexander, D., & Gilbert, H. R. 2007c, ApJ, 661, 1260
Liu, Y., & Zhang, H. 2001, A&A, 372, 1019
Masuda, S., Kosugi, T., Hara, H., Tsuneta, S., & Ogawara, Y. 1994, Nature, 371, 495
Moore, R. L., Sterling, A. C., Hudson, H. S., & Lemen, J. R. 2001, ApJ, 552, 833
Priest, E. R., & Forbes, T. G. 2002, A&AR, 10, 313
Romano, P., Contarino, L., & Zuccarello, F. 2003, Sol. Phys., 214, 313
Sui, L., & Holman, G. D. 2003, ApJ, 596, L251
Temmer, M., Veronig, A. M., Vrsnak, B., Rybak, J., Gomory, P., Stoiser, S., & Maricic, D. 2008, ApJ, 673, L95
Török, T., & Kliem, B. 2003, A&A, 406, 1043
Török, T., & Kliem, B. 2005, ApJ, 630, L97
van Ballegooijen, A. A., & Martens, P. C. H. 1990, ApJ, 361, 283
Williams, D. R., Torok, T., Demoulin, P., van Driel-Gesztelyi, L., & Kliem, B. 2005, ApJ, 628, L163
Zhang, J., & Dere, K. P. 2006, ApJ, 649, 1100
Zhang, J., Dere, K. P., Howard, R. A., Kundu, M. R., & White, S. M. 2001, ApJ, 559, 452
Zhang, J., Dere, K. P., Howard, R. A., & Vourlidas, A. 2004, ApJ, 604, 420